Discrete Ultra-Broadband Perfect Anomalous Reflection in Depth Gradient Metasurfaces

Siyu Gu(顾思瑜)[1†], Cong Wang(王聪)[1†], Ziying Gao(高紫莹)[1], Lei Gao(高雷)[1,2], Drolgar(卓嘎)[3*], Feng Gao(高峰)[1*], Shaojun Wang(王绍军)[4*], and Yadong Xu(徐亚东)[1*]

[1]*School of Physical Science and Technology & Jiangsu Key Laboratory of Frontier Material Physics and Devices, Soochow University, Suzhou 215006, China*
[2]*School of Optical and Electronic Information & Jiangsu (Suzhou) Key Laboratory of Biophotonics, Suzhou City University, Suzhou 215104, China*
[3]*School of Science, Lasa Normal University, Lasa 850007, China*
[4]*School of Optoelectronic Science and Engineering, Soochow University, Suzhou 215006, China*

(Received 8 May 2025; accepted manuscript online 8 July 2025)

Perfect anomalous reflections have been demonstrated in optical phase gradient metasurfaces (PGMs), but they suffer from single-frequency (narrow-band) response due to the intrinsic limitation of natural geometric periodicity. Here, we provide both numerical and analytical evidence that a depth gradient metasurface can achieve discrete ultra-broadband perfect anomalous reflection in the microwave range in the absence of geometric periodicity. Remarkably, by adjusting the operating frequency of the incident wave, the same effect can be steadily obtained via a physically equivalent phase periodicity in the PGM. Based on this mechanism, a perfect retroreflector with a broadband response ranging from 1 GHz to 40 GHz is realized. Our work has promising applications in communication, source tracking, and military satellites.

DOI: 10.1088/0256-307X/42/9/090401 CSTR: 32039.14.0256-307X.42.9.090401

Optical metasurfaces have become a powerful platform for manipulating light fields and play a significant role in classical and quantum optics.[1–5] In particular, phase gradient metasurfaces (PGMs) can physically introduce the degrees of freedom of phase gradients, which provide a novel approach to manipulating light transmission and wavefront, yielding a variety of promising applications in photonics and integrated photonics.[6–29] Examples include optical holograms,[6,7] metalens,[8–10] wavefront control,[11–20] vortex generation,[21–23] quantum light sources,[24–26] and nonlinear optics.[27–29] Due to the general nature of waves, the concept of PGM was subsequently extended from optics to other wave systems, such as acoustic waves.[30–34] Although much progress has been made in this regard, the majority of PGM-based devices reported so far—whether in optics or other wave systems—show an inherent shortcoming of single-frequency response, limiting their applications in many fields such as energy conversion, nonlinear optics, quantum light sources, and so on. Although the tolerance in PGM design often allows for a certain amount of bandwidth; in many cases the bandwidth is still too narrow to satisfy the requirements.[35] Recently, some studies have focused on achromatic and dispersion control to design PGMs with broadband responses.[36–40] However, these methods are only applicable to specific meta-atoms and designs that are not generally applicable.

The aim of this work is to reveal the mechanism for achieving distinct PGMs with broadband response. Geometrically, a typical PGM is a periodically array of supercells consisting of m unit cells (m is an integer) with different scattering responses. These unit cells discretely introduce an abrupt phase shift (APS) covering 2π over the supercell, thereby inducing a phase gradient along the interface of two media. The geometric periodicity of PGM is the fundamental reason of its single frequency response. Here, we design and explore a reflection-type PGM that lacks geometric periodicity while retaining the phase gradient. Specifically, the reflection-type PGM consists of subwavelength metallic air grooves modulated with a well-defined gradient depth [see Fig. 1(a)], and it is originally designed to operate at 10 GHz. We will show that although geometric periodicity is removed, the phase periodicity can enable the same anomalous diffraction of reflection as those in typical PGMs with geometric periodicity. As the operating frequency changes, the APS varies linearly with frequency synchronously, which give rise to the phase period length spanning a different number of unit cells, physically guaranteeing an ultra-broadband response with discrete characteristics in the range 1–40 GHz. A simple theory is developed to predict these outcomes. Moreover, for the application, we show that this PGM can act as a broadband perfect microwave retroreflector, i.e., the reflected light returns back to the same direction as the incidence.[41–49] Our work provides a novel approach to designing broadband PGM-based devices. These findings have potential

†These authors contributed equally to this work.
*Corresponding authors. Email: zhuogar@126.com; fenggao@suda.edu.cn; swang.opto@suda.edu.cn; ydxu@suda.edu.cn
© 2025 Chinese Physical Society and IOP Publishing Ltd. All rights, including for text and data mining, AI training, and similar technologies, are reserved.

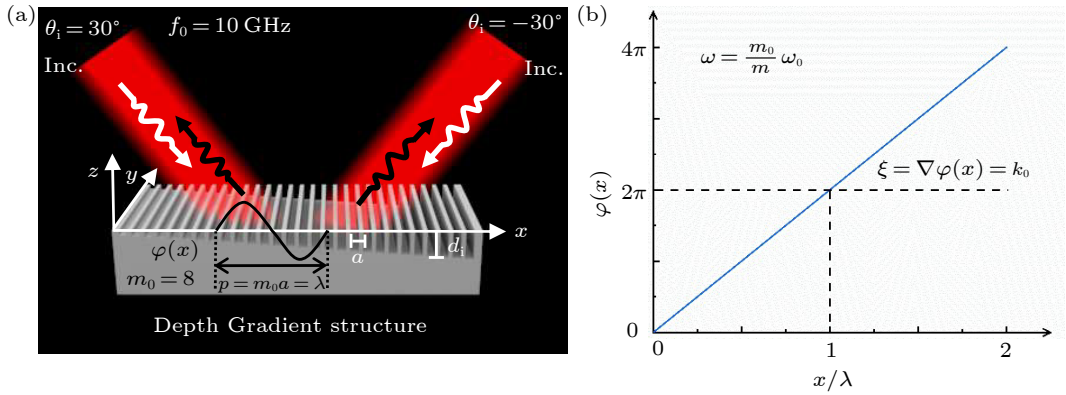

Fig. 1. (a) Schematic diagram of a depth-gradient metagrating in air, featuring a structure composed of air grooves $N = 240$ with the depth of $d_1, d_2, \ldots, d_N$ as indicated. The interval of adjacent air grooves is $\Delta d = \lambda_0/2m_0 = 1.875$ mm. The designed depth of the air grooves is supported by $d_i = d_1 + (i-1)\Delta d$ with $d_1 = 30$ mm. Under the initial frequency $\omega_0/2\pi = 10$ GHz, the APS of 2π is introduced in Fig. 1(b), and the number of air grooves covering a phase shift of 0–2π is $m_0 = 8$. (b) Reflected APS changes as air grooves vary continuously. At the initial target frequency, the phase gradient of this depth gradient structure is $\xi = k_0$. When the working frequency changes as $\omega = m_0\omega_0/m$, the phase gradient remains unchanged, where m is the number of air grooves covering a 2π phase shift, and its range is $m \in [2, 120]$.

applications in microwave or millimeter wave communication devices such as remote sensing, source tracking, and military satellites.

Figure 1(a) shows the schematic of the depth gradient metasurface (DGM), which is composed of a metal substrate engraved with subwavelength metal grooves. All grooves harbor the identical width and separation, while their depth is monotonically and linearly changing. A TM-polarized plane wave (with its magnetic field oriented along the y-direction) obliquely incident on the designed DGM. Originally, the operating frequency is 10 GHz (corresponding to a wavelength of $\lambda_0 = 30$ mm). In this case, the metal behaves as a perfect electric conductor, allowing all grooves to function as ideal subwavelength waveguides that support only the fundamental guided mode. For geometry parameters, the separation width and depth of the grooves are $a = \lambda_0/8$ and $w = 0.8a$. The depth of grooves is determined based on the phase shift of the wave propagating within the air groove, i.e., $2k_0\Delta d = 2\pi/m_0$, where k_0 is the wave vector in air. Accordingly, the depth of the ith groove is given by $d_i = d_1 + (i-1)\Delta d$, where $i = 1, \ldots, N$, $\Delta d = \lambda_0/16$, and $N = 240$ (the total number of grooves). As the incident wave approaches the air grooves and reflects back at the air-DGM interface, an APS is introduced along the x-direction, which is given by $\varphi(x, \omega_0) = 2k_0 d_i + \phi_0$, and $k_0 = 2\pi/\lambda_0$ is the wave vector and ϕ_0 is the initial phase determined by the DGM structure as well asthe incident angle. The APS is in fact the accumulated propagation phase, which varies linearly with both the operating frequency and spatial position, as depicted in Fig. 1(b). At the given frequency $\omega_0/2\pi = 10$ GHz, each 2π period of APS involves $m_0 = 8$ groove number, with the phase difference between two adjacent grooves being $\Delta\varphi = \pi/4$. The geometric length of a phase period is $p = m_0 a$. Consequently, based on the concept of PGMs,[11] the phase gradient introduced by the APS at the operating frequency $\omega_0/2\pi = 10$ GHz is expressed as $\xi = \nabla\varphi(x) = k_0$.

The DGM exhibits the same anomalous diffraction in reflection as traditional PGMs with supercells, despite the absence of geometric periodicity. This diffraction rule is governed by[12,15,16]

$$\sin\theta_r = \sin\theta_i + n\frac{\xi(\omega_0)}{k_0}, \tag{1}$$

where θ_i and θ_r are the incident and reflection angles, respectively, and n is an integer indicating the diffraction order. Based on previous results,[12,15] for $\theta_i < 0$, $n = 1$; for $\theta_i > 0$, $n = -1$. This means that perfect anomalous reflections occur for all incidence angles, i.e., $\theta_i\theta_r < 0$. Specifically, when $\theta_i = -\theta_r$, it corresponds to retroreflection, which means that the refection wave returns exactly in the incidence direction. In this way, the retroreflection angle is

$$\sin\theta_i^{re} = \frac{n}{2}\frac{\xi(\omega_0)}{k_0}. \tag{2}$$

Since $\xi = k_0$, we obtain $\theta_i^{re} = \pm 30°$.

These theoretical predictions are confirmed by the numerical results based on full wave simulations, as shown in Fig. 2. Figure 2(a) illustrates the relationship between the diffraction efficiency (i.e., reflectivity) and the incident angle for the $n = 1$ and $n = -1$ diffraction orders. For $\theta_i < 0$, the $n = 1$ diffraction order dominates the reflected wave, achieving perfect reflective diffraction and maximum reflectivity at $\theta_i = -30°$. Conversely, for $\theta_i > 0$, the $n = -1$ diffraction order becomes predominant, with perfect reflective diffraction and maximum reflectivity occurring at $\theta_i = 30°$. Moreover, figure 2(b) shows the spatial phase distribution of the diffraction field at the air-DGM interface, where the blue curve is for $\theta_i = -30°$ corresponding to $n = 1$ order, and the red is for $\theta_i = 30°$ corresponding to the $n = -1$ order. In this case, the incident direction opposes the phase gradient's direction, leading to an increasing phase delay. Conversely, when $\theta_i = 30°$ (i.e., $n = -1$), the incident direction aligns with the phase gradient's direction, resulting in a decreasing phase delay.

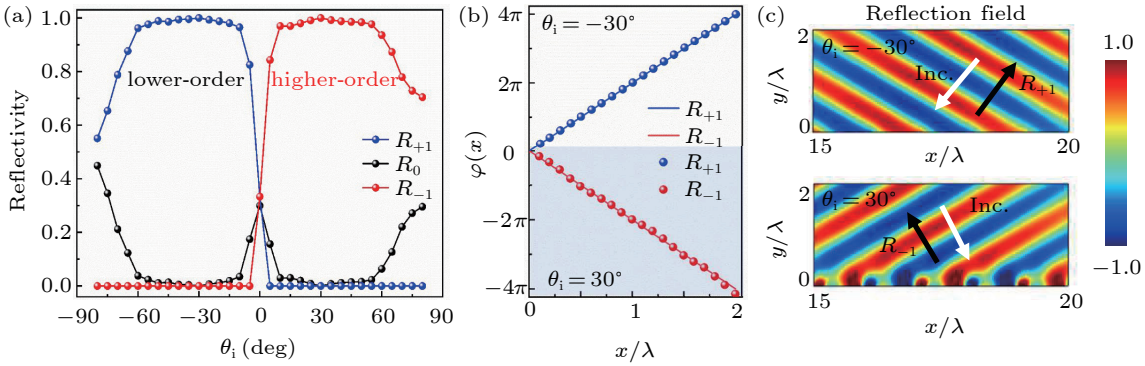

Fig. 2. (a) Relationship between reflectivity and incident angles, with the black, blue, and red curves representing the reflection of orders $n = 0$, $n = 1$, and $n = -1$, respectively. (b) Reflection phase retardation at the air grating interface over two phase periods when $\theta_i = -30°$ (blue) and $\theta_i = 30°$ (red) for $m_0 = 8$, with a working wavelength of $\lambda_0 = 30\,\text{mm}$ and a period length $p = \lambda_0$. Analytical results are shown by the curves, while the circles represent numerical calculations. (c) Reflected field patterns for $\theta_i = -30°$ and $\theta_i = 30°$ under an incident frequency of 10 GHz.

It is evident that the phase delay no longer exhibits a folded phase behavior. Figure 2(c) shows the corresponding reflected patterns for $\theta_i = \pm 30°$, confirming the occurrence of perfect retroreflection. These results demonstrate that even in the absence of structural periodicity, the DGM still exhibits anomalous diffraction, following the same diffraction principles as conventional PGMs with periodic supercells. This behavior arises due to the intrinsic periodicity of the APS.

Different from the typical PGMs with periodic supercells, the DGM provides a platform for achieving a broadband response. For the fixed DGM geometry, as mentioned above, at the initial design frequency ω_0, the spatial APS is $\varphi(x, \omega_0) = 2\omega_0 d_i/c + \phi_0$, where ϕ_0 is initial phase of a constant, which is a linear function of the depth, thanks to the linear dispersion of subwavelength air grove. As the incident working frequency changes, the APS at arbitrary frequency ω becomes

$$\varphi(x, \omega) = \frac{\omega}{\omega_0}\varphi(x, \omega_0) + \phi_0', \tag{3}$$

where ϕ_0' is another initial phase. Moreover, based on $\nabla\varphi(x, \omega)$, the phase gradient at a given working frequency is

$$\xi(\omega) = \frac{\omega}{\omega_0}\frac{\partial\varphi(x, \omega_0)}{\partial x} = \frac{\omega}{c}, \tag{4}$$

which coincides with the wave vector of the incident wave. This implies that the DGM structure is dispersionless, and the diffraction at a given working frequency ω is still governed by Eq. (1), resulting in the same anomalous reflection, in other words, a broadband response is achieved.

It should be noted that the 2π phase periodicity is another condition that limits the broadband response. As the frequency changes, the changed APS requires different groove number in 2π phase. Obviously, such broadband response is not continuous but discrete. Based on design principle of PGMs, the minimum number of meta-atoms for introducing APS of full 2π is $m = 2$, i.e., $m \geqslant 2$. The DGM with $m = 1$ reduces to the common grating without phase gradient. Thus, in this design, it has $m \in [2, N]$. Then the working frequency of the fixed DGM is

$$\omega = \frac{m_0}{m}\omega_0. \tag{5}$$

For instance, when $m = 4$, the corresponding working frequency becomes $\omega/2\pi = 20\,\text{GHz}$. Moreover, based on the condition $m \in [2, N]$, the working bandwidth range is $\omega \in [\omega_{\min}, \omega_{\max}]$, where $\omega_{\min} = m_0\omega_0/N$ and $\omega_{\max} = m_0\omega_0/2$. The frequency interval is

$$\Delta\omega = \frac{m_0}{m(m+1)}\omega_0. \tag{6}$$

When $m \gg m_0$, then $\Delta\omega \to 0$, which means the broadband frequency becomes quasi-continuous. In this designed DGM, the maximum operating frequency is $\omega_{\max}/2\pi = 40\,\text{GHz}$, and the minimum operating frequency is $\omega_{\min}/2\pi = 0.33\,\text{GHz}$. In addition, the total number of air grooves can be infinite (i.e., $N \to \infty$), causing the minimum working frequency to approach an extremely low frequency (i.e., $\omega_{\min} \to 0$).

To illustrate this, several cases with $m = 2$, 5, 8, 10, and 16 were explored to demonstrate the broadband response of the DGM. Figure 3(a) presents the relationship between the APS and the number of air grooves per phase period, as described by Eq. (3). It is evident that in our design, by varying the number of air grooves per phase period, the phase periodicity can be modulated. Consequently, the APS exhibits a continuous linear variation with different slopes, corresponding to different phase gradient amplitudes. Figure 3(b) displays the corresponding incident working frequencies of 40, 16, 10, 8, and 5 GHz, which are in excellent agreements with the theoretical predictions based on Eq. (5). In addition, we also examined other values of m, and the achieved results agree with theoretical predictions well [see the circles in Fig. 3(b)]. It can be observed that as the number of unit cells within one phase period increases, the corresponding incident frequencies become more densely packed, further revealing the broadband feature of the DGM. To validate these findings, we performed numerical simulation by harnessing COMSOL Multiphysics, and the incident wave is set as a Gaussian beam with a waist width of eight wavelengths.

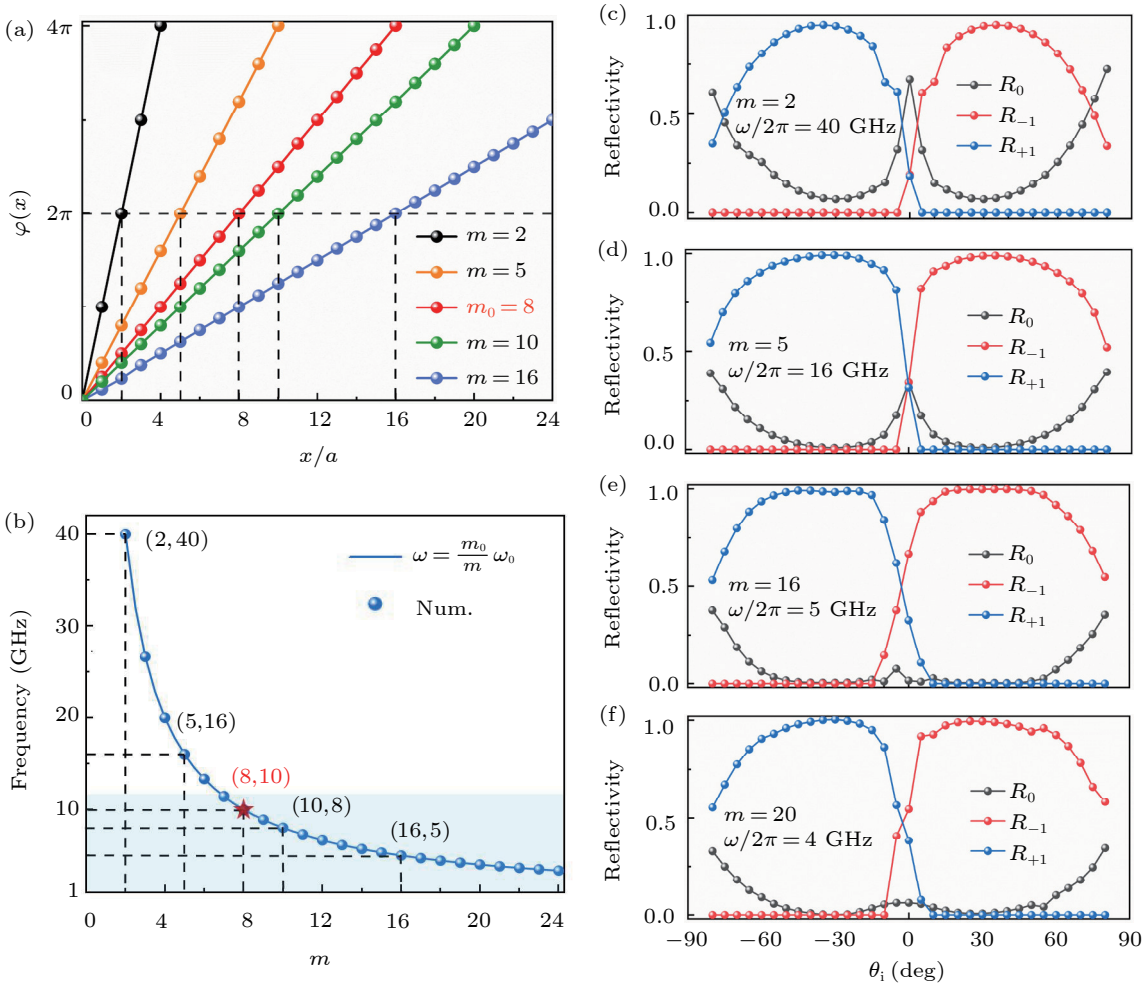

Fig. 3. Broadband response of a fixed DGM structure demonstrating perfect anomalous reflection under varying operating frequencies. (a) Relationship between the phase delay and the number of air grooves. Each point represented by a circle, corresponds to the position of an air groove in each configuration. (b) Operating frequency ranging from 1 GHz to 40 GHz, as the integer m changes from 2 to 24. The initial design frequency of 10 GHz is marked by a red star. (c)–(f) Reflectivity in each diffraction order versus incident angle for different m when the structure is fixed. Specifically: (c) $m=2$, $\omega/2\pi=40$ GHz, (d) $m=5$, $\omega/2\pi=16$ GHz, (e) $m=16$, $\omega/2\pi=5$ GHz, (f) $m=20$, $\omega/2\pi=4$ GHz. In all cases, the black, blue, and red curves represent the reflection orders $n=0$, $n=1$, and $n=-1$, respectively.

Figures 3(c)–3(f) show the numerically calculated diffraction efficiency for all diffraction orders under different incident frequencies for the fixed DGM structure. Obviously, the same anomalous reflection phenomena occur across all incident frequencies. These behaviors are consistent with the initially designed case of $m_0=8$. Specifically, when the incident angle is smaller than the critical angle, the reflected wave is dominated by the $n=1$ diffraction order; whereas when the incident angle exceeds the critical angle, the $n=-1$ diffraction order becomes dominant. This clearly demonstrates the ultra-broadband perfect anomalous reflection performance achieved by the DGM structure. Notably, due to the finite incident beam employed in simulations, the theoretical minimum limiting frequency is difficult to achieve. This is because, at the theoretical minimum limiting frequency, there is only one phase period in this gradient structure, in which the diffraction and interference of the wave are destroyed. In practice, it is numerically found that when $m=120$, the anomalous diffraction phenomena in DGM can be maintained very well, consequently, the actual minimum operating frequency is $\omega_{\min}/2\pi=0.67$ GHz in this design case.

The designed DGM and its associated diffraction physics provide a way to design perfect retroreflector with a broadband response. Figure 4(a) shows the spectrum of retroreflection efficiency when a Gaussian beam with an incident angle of $|\theta_i|=30^\circ$ is incident obliquely to the DGM. Therein, the retroreflection efficiency is defined by the ratio of the retroreflection power to the total incident power. As the finite-width Gaussian beam is used in the numerical calculations, the retroreflection power is obtained by integrating the reflected energy within the range of $|\theta_r|=30^\circ\pm2^\circ$. It is evident that a series of discrete resonant peaks can be seen from the spectrum. Specifically, with a frequency range of 1–40 GHz, discrete broadband retroreflection can be achieved with an efficiency of exceeding 95%. Figure 4(b) illustrates the reflection field patterns for $m=2$, 5, 16, and 20 when $\theta_i=30^\circ$, which

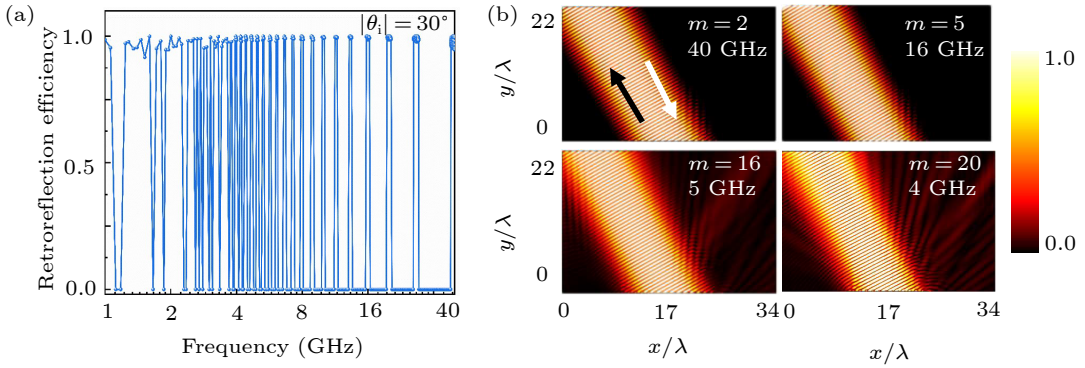

Fig. 4. Discretely broadband perfect retroreflection. (a) Numerical calculated efficiency of perfect retroreflection in the frequency range [1 GHz, 40 GHz]. (b) Field distribution of reflection field for different incident frequency incident to the fixed DGM.

illustrates perfect retroreflection performance. This discrete property further reveals that the diffraction properties and physics of PGM are determined by the integer property of m.

In summary, inspired by the concept of the PGMs, we have designed and investigated a DGM without geometric periodicity operating at a frequency of 10 GHz, but the phase gradient is retained. We have showed that due to the phase periodicity, the same anomalous diffraction happens in the DGM as those in typical PGMs with geometric periodicity. The phase periodicity is a linear function of both spatial position and operating frequency, ensuring that the DGM has the same anomalous diffraction with an ultra-broadband response ranging from 1 GHz to 40 GHz. As the phase periodicity is dependent of the integer property of m, such ultra-broadband response is discrete rather than continuous, and the discrete interval frequency is determined by m. All these results have been confirmed by theoretical analysis and full wave simulations. Furthermore, we have demonstrated that the DGM achieves over 95% retroreflection efficiency at multiple discrete frequency points. Thanks to the linear dispersion of subwavelength air groves, the design method we proposed for the microwave regime can also be extended to other high frequencies, such as terahertz frequency or infrared optical regime. Compared with the previous methods for broadband response, our works provides a unique approach to design ultra-broadband PGM-based devices with discrete or quasi-continuous features, and the bandwidth can be tuned by the number m of unit cells in the supercell. Our work has promising applications in microwave and millimeter-wave communication, remote sensing, laser tracking, and military satellites.

Acknowledgements. This work was supported by the National Natural Science Foundation of China (Grant Nos. 12274313, 62275184, and 62411540033), Collaborative Innovation Center of Suzhou Nano Science and Technology, Suzhou Basic Research Project (Grant No. SJC2023003), the Gusu Leading Talent Plan for Scientific and Technological Innovation and Entrepreneurship (Grant No. ZXL2024400), and the Priority Academic Program Development of Jiangsu Higher Education Institutions.

References

[1] Yu N and Capasso F 2014 *Nat. Mater.* **13** 139
[2] Xu Y, Fu Y, and Chen H 2016 *Nat. Rev. Mater.* **1** 16067
[3] Sun S, He Q, Hao J, Xiao S, and Zhou L 2019 *Adv. Opt. Photonics* **11** 380
[4] Vabishchevich P and Kivshar Y 2023 *Photonics Res.* **11** B50
[5] Ji W, Chang J, Xu H X, Gao J R, Gröblacher S, Urbach H P, and Adam A J L 2023 *Light: Sci. Appl.* **12** 169
[6] Genevet P, Lin J, Kats M A, and Capasso F 2012 *Nat. Commun.* **3** 1278
[7] So S, Kim J, Badloe T, Lee C, Yang Y, Kang H, and Rho J 2023 *Adv. Mater.* **35** 2208520
[8] Wang S, Wu P C, Su V C, Lai Y C, Chen M K, Kuo H Y, Chen B H, Chen Y H, Huang T T, Wang J H, Lin R M, Kuan C H, Li T, Wang Z, Zhu S, and Tsai D P 2018 *Nat. Nanotechnol.* **13** 227
[9] Wang Y, Chen Q, Yang W, Ji Z, Jin L, Ma X, Song Q, Boltasseva A, Han J, Shalaev V M, and Xiao S 2021 *Nat. Commun.* **12** 5560
[10] Barulin A, Kim Y, Oh D K, Jang J, Park H, Rho J, and Kim I 2024 *Nat. Commun.* **15** 26
[11] Yu N, Genevet P, Kats M A, Aieta F, Tetienne J P, Capasso F, and Gaburro Z 2011 *Science* **334** 333
[12] Xu Y, Fu Y, and Chen H 2015 *Sci. Rep.* **5** 12219
[13] Mohammadi Estakhri N and Alù A 2016 *Phys. Rev. X* **6** 041008
[14] Estakhri N M, Neder V, Knight M W, Polman A, and Alù A 2017 *ACS Photonics* **4** 228
[15] Cao Y, Fu Y, Zhou Q, Ou X, Gao L, Chen H, and Xu Y 2019 *Phys. Rev. Appl.* **12** 024006
[16] Fu Y, Shen C, Cao Y, Gao L, Chen H, Chan C T, Cummer S A, and Xu Y 2019 *Nat. Commun.* **10** 2326
[17] Cao Y, Yu B, Fu Y, Gao L, and Xu Y 2020 *Chin. Phys. Lett.* **37** 097801
[18] Cao Y, Fu Y, Jiang J H, Gao L, and Xu Y 2021 *ACS Photonics* **8** 2027
[19] Zhang T, Zheng C, Chen Z N, and Qiu C W 2022 *Nano Lett.* **22** 5607
[20] Cao Y, Fu Y, Gao L, Chen H, and Xu Y 2023 *Phys. Rev. A* **107** 013509
[21] Ahmed H, Kim H, Zhang Y, Intaravanne Y, Jang J, Rho J, Chen S, and Chen X 2022 *Nanophotonics* **11** 941
[22] Ren H, Briere G, Fang X, Ni P, Sawant R, Héron S, Chenot S, Vézian S, Damilano B, Brändli V, Maier S A, and Genevet P 2019 *Nat. Commun.* **10** 2986
[23] Chen Q, Qu G, Yin J, Wang Y, Ji Z, Yang W, Wang Y, Yin Z, Song Q, Kivshar Y, and Xiao S 2024 *Nat. Nanotechnol.* **19** 1000

[24] Li L, Liu Z, Ren X, Wang S, Su V C, Chen M K, Chu C H, Kuo H Y, Liu B, Zang W, Guo G, Zhang L, Wang Z, Zhu S, and Tsai D P 2020 *Science* **368** 1487

[25] Solntsev A S, Agarwal G S, and Kivshar Y S 2021 *Nat. Photonics* **15** 327

[26] Ma J, Zhang J, Horder J, Sukhorukov A A, Toth M, Neshev D N, and Aharonovich I 2024 *Adv. Mater.* **36** 2313589

[27] Zhou Q, Fu Y, Liu J, Yan H, Chen H, Gao L, Jiang J, and Xu Y 2022 *Adv. Opt. Mater.* **10** 2201590

[28] Zhang Z, Xu C, Liu C, Lang M, Zhang Y, Li M, Lu W, Chen Z, Wang C, Wang S, and Li X 2023 *Nano Lett.* **23** 7584

[29] Rong R, Li Y, Wang M, Tang Y, Xu H, Li K, Li G, Cao T, and Chen S 2023 *ACS Photonics* **10** 3248

[30] Assouar B, Liang B, Wu Y, Li Y, Cheng J C, and Jing Y 2018 *Nat. Rev. Mater.* **3** 460

[31] Wang X, Dong R, Li Y, and Jing Y 2023 *Rep. Prog. Phys.* **86** 116501

[32] Zhang K, Li X, Dong D, Xue M, You W, Liu Y, Gao L, Jiang J, Chen H, Xu Y, and Fu Y 2023 *Adv. Sci.* **10** 2304992

[33] Quan J, Sun B, Fu Y, Gao L, and Xu Y 2024 *Chin. Phys. Lett.* **41** 014301

[34] Fang X, Li S, Sun B, Yan D, Yang J, Luo J, Gao D, and Xu Y 2025 *Chin. Phys. Lett.* **42** 034301

[35] Cao X, Wang Q, Wan P, Zhang W, Lin Z, Chui S T, and Du J 2020 *Adv. Opt. Mater.* **8** 2000452

[36] Asadchy V S, Díaz-Rubio A, Tcvetkova S N, Kwon D H, Elsakka A, Albooyeh M and Tretyakov S A 2017 *Phys. Rev. X* **7** 031046

[37] Cheng Q, Ma M, Yu D, Shen Z, Xie J, Wang J, Xu N, Guo H, Hu W, Wang S, Li T, and Zhuang S 2019 *Sci. Bull.* **64** 1525

[38] Zang W, Yuan Q, Chen R, Li L, Li T, Zou X, Zheng G, Chen Z, Wang S, Wang Z, and Zhu S 2020 *Adv. Mater.* **32** 1904935

[39] Gao Y, Quan J, Sun B, Xu L, Fu Y, Chen H, and Xu Y 2024 *Appl. Phys. Lett.* **124** 191701

[40] Quan J, Xu L, Fu Y, Gao L, Chen H, and Xu Y 2024 *J. Acoust. Soc. Am.* **156** 2982

[41] Li Z, Palacios E, Butun S, and Aydin K 2015 *Nano Lett.* **15** 1615

[42] Arbabi A, Arbabi E, Horie Y, Kamali S M, and Faraon A 2017 *Nat. Photonics* **11** 415

[43] Shen C, Díaz-Rubio A, Li J, and Cummer S A 2018 *Appl. Phys. Lett.* **112** 183503

[44] Yan L, Zhu W, Karim M F, Cai H, Gu A Y, Shen Z, Chong P H J, Kwong D, Qiu C, and Liu A Q 2018 *Adv. Mater.* **30** 1802721

[45] Fu Y, Cao Y, and Xu Y 2019 *Appl. Phys. Lett.* **114** 053502

[46] Yang W, Chen K, Zheng Y, Zhao W, Hu Q, Qu K, Jiang T, Zhao J, and Feng Y 2021 *Adv. Sci.* **8** 2100885

[47] Tan Q, Zheng B, Cai T, Qian C, Zhu R, Li X, and Chen H 2022 *Adv. Sci.* **9** 2201397

[48] Wei W Y, Shi Y, Meng Z K, Hui R, and Wu Q W 2024 *Nanophotonics* **13** 3737

[49] Chen Y, Quan J, Gao Y, Sun B, Gao F, Fu Y, and Xu Y 2025 *Appl. Phys. Lett.* **126** 201704